であった．また，相関係数が 0.996 と，距離と半値幅の間には高い直線関係があることを確認できた．

2）ファントム実験

Fig. 6 に，コリメータ開口補正を行わなかった場合と行った場合の複数線線源ファントムの再構成画像を，**Table 1** に線線源の半値幅を示す．コリメータ開口補正によって，コリメータ開口補正を行わなかった場合 8.8mm だった解像度が 3.5mm に改善した．また，視野内での変動は 0.2 mm であった．

Table 2 に，濃度一様プールファントムの再構成画像の CoV を示す．吸収補正・散乱線補正による CoV の向上が確認できた．10% 程度の範囲で画像カウントが一様であった．

Fig. 7 に，2D 脳ファントム再構成画像およびラインプロファイルを示す．また，**Table 3** に，灰白質と白質の局所間カウント比および全灰白質領域と全白質領域のカウント比を示す．灰白質と白質の局所間カウント比では，GM1/WM1 のような構造の大きい領域において，AC+SC の効果はみられたが，構造の小さい領域においては，AC+SC の効果はみられなかった．解像度補正を加えた AC+SC+CDRC によって構造の小さい領域でも改善が見られ，比較的構造の大きい領域では，真の比率である 4 に近い値となった．全灰白質領域と全白質領域のカウント比は，補正なしでは 2.6，AC+SC で 2.7，AC+CDRC で 3.1，AC+SC+CDRC で 3.5 となった．本手法によって放射能濃度の比例性は大きく改善され，真の比率 4 にもっとも近く，その誤差は 12% 程度であった．このことは画像コントラストが改善したこ

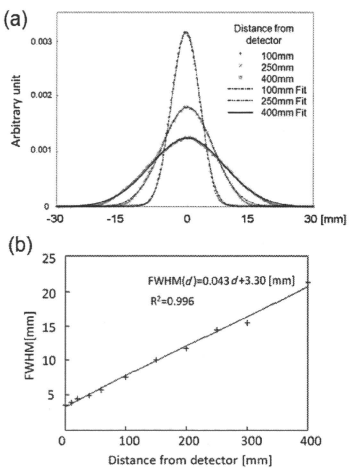

Fig. 5 Collimator response function for Toshiba GCA7200-A with LEHR collimator and ^{99m}Tc. (a) Full width at half maximum as a function of distance from the detector. (b) Collimator response functions at the locations 100 mm, 250 mm and 400 mm distant from detector.

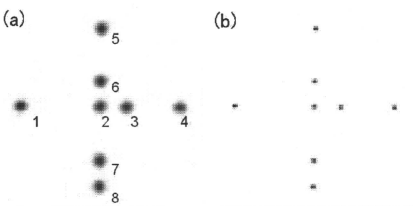

Fig. 6 Reconstructed images of multi-line sources phantom. (a) without CDRC, (b) with CDRC.

Table 1 FWHMs of reconstructed image [mm].

No. of source	Without CDRC	With CDRC
1	8.6	3.2
2	9.1	3.8
3	8.8	3.5
4	8.7	3.3
5	8.4	3.3
6	8.8	3.7
7	9.0	3.5
8	8.7	3.3
	8.8 ± 0.2	3.5 ± 0.2

Table 2 CoVs of the reconstructed images of the uniform cylindrical phantom.

	No compensation	AC	AC+SC	AC+CDRC	AC+SC+CDRC
CoV[%]	13.3	10.5	9.9	10.2	9.7

Table 3 Count ratio of gray-to-white matter on the reconstructed image of 2D brain phantom.

	True	No compensation	AC+SC	AC+CDRC	AC+SC+CDRC
GM1/WM1	4.0	2.4	2.9	3.1	4.0
GM1/WM2		1.8	1.7	1.8	1.9
GM1/WM3		1.6	1.7	1.8	2.4
GM2/WM1		2.0	1.8	3.3	4.3
GM2/WM2		1.4	1.1	1.9	2.1
GM2/WM3		1.3	1.1	1.9	2.6
GM3/WM1		2.5	2.5	2.6	4.1
GM3/WM2		1.9	1.4	1.6	1.9
GM3/WM3		1.7	1.4	1.6	2.5
Whole GM/WM	4.0	2.6	2.7	3.1	3.5

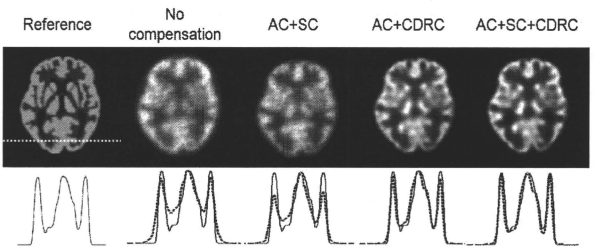

Fig. 7 Reconstructed images (top row) and horizontal profiles across each with reference profile (bottom row) of 2D brain phantom. Reference is digital image blurred by 3.5mm FWHM Gaussian filter.

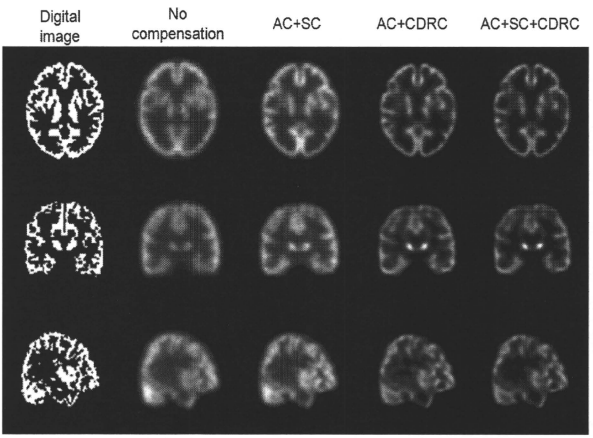

Fig. 8 Reconstructed images of 3D brain phantom. (top row) Transverse. (middle row) Coronal. (bottom row) Sagittal.

とも意味する．また，**Fig. 7** の再構成画像のプロファイル比較で，本手法によるプロファイルが真のプロファイルにきわめてよく一致していることが確認できた．

Fig. 8 に，3D 脳ファントム再構成画像を示す．コリメータ開口補正および散乱線補正による，解像度およびコントラストが 3 次元的に改善されていることが確認できた．

Fig. 9 に，コリメータ開口補正を行わなかった場合と，コリメータ開口補正を行った場合で画像再構成の反復回数を変えたときの線線源の解像度と 3D 脳ファントムの CoV との関係を示す．コリメータ開口補正を行って解像度 3.5mm 同程度の場合，CoV はコリメータ開口補正を行わない場合と同程度あるいはそれ以下であった．一方，コリメータ開口補正を行った場合の解像度をコリメータ開口補正無しの場合と同程度にすると，CoV はコリメータ開口補正を行わなかった場合よりも大きく低下していた．

Fig. 10 に，コリメータ開口補正を行なわなかった場合および行った場合の 1 フレームの画像再構成とフレーム間の CoV 画像を示す．CoV 画像は見やすくするために，3D 脳ファントムの領域外の値は 0 とした．コリメータ開口補正を行った場合の再構成画像と CoV 画像は，コリメータ開口補正無しの解像度 8.1mm と同程度の 7.2mm となる反復回数 2 回のものを示した．コリメータ開口補正を行った場合の CoV は，行わなかった場合に比べて，大きく低下し，視床，脳室ともに 21% 程度の値まで改善した．この結果からコリメータ開口補正は，解像度改善効果があるだけでなく，雑音抑制効果もあるといえる．

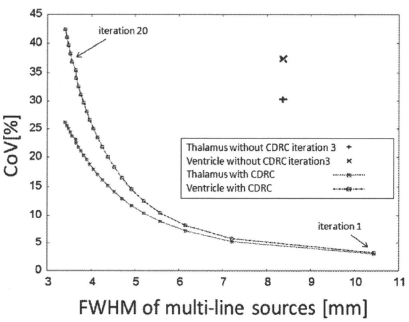

Fig. 9 CoV as a function of spatial resolution in the reconstruction with/without CDRC. The CoV and the FWHM of line source are indices of noise and spatial resolution, respectively. The CoVs in thalamus and ventricle regions on CoV images of 3D brain phantom and the FWHMs of line source images reconstructed were examined for each number of iterations.

5. 考　察

本画像再構成法のコリメータ開口補正によって，コリメータ開口補正を行わなかった場合 8.8 mm だった解像度が 3.5 mm と大きく改善した．解像度の改善は脳ファントムの再構成画像からも明らかであった．定量評価の前提となる，濃度一様ファントムの再構成画像の一様性に関しても，10% 程度の範囲で一様であることが確認できた．

画像コントラストでもある放射能濃度比率の再現性に関しては，吸収・散乱補正で改善され，コリメータ開口補正を加えることでさらに改善された．ただし，構造の小さい局所領域では吸収・散乱補正だけではほとんど改善されていなかった．これはコリメータ開口補正が解像度の改善だけでなく，部分容積効果の影響を改善する効果もあり，とくに構造の小さい局所領域での定量解析に有効であるといえる．比較的大きな構造の領域では真の比率が再現できており，全灰白質と全白質との放射能濃度の比例性でも，部分容積効果の影響はあるものの，誤差は 12% 程度まで改善され，高い精度で定量性が確

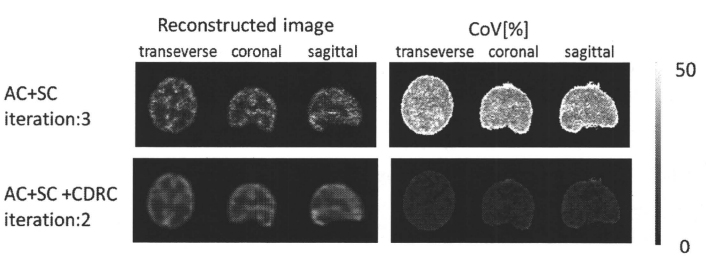

Fig. 10 Comparison of noise indices in the 3D brain phantom images reconstructed with/without CDRC. (left) Reconstructed images of first frame. (right) CoV images.

保されることが示唆された．これは，画像コントラストが大きく改善されたことも意味する．

Fig. 8 において，コリメータ開口補正を行った場合，コロナル像において線条体部分が他の領域に比べて高カウントとなっていた．これは線条体部分が他の領域に比べて大きいため，部分容積効果に対する補正効果が他の小さい領域に比べ大きいためであると考えられる．2D 脳ファントムにおいても，比較的大きな構造の領域では真の比率が再現できているのに対し，構造の小さい領域では，大きな領域よりも部分容積効果の影響を受けている．

また，コリメータ開口補正を行った場合，コリメータ開口補正を行わなかった場合よりも高解像度で，かつ低雑音な画像が得られることが確認できた．コリメータ開口補正なしの場合と同程度の解像度が得られる反復回数で画像再構成した場合，大きく雑音が抑制され，同程度の雑音となる反復回数で画像再構成した場合，解像度が高くなることが確認できた．この結果から，OS-EM のような逐次近似画像再構成に正確なコリメータぼけモデルを組み込んだ場合，解像度の改善だけでなく，信号対雑音比（signal-to-noise ratio; SNR）も向上する〔10〕ことが本研究でも確認できた．

本研究ではエミッション画像から輪郭を抽出し，輪郭内に均一な吸収係数をあてはめることにより吸収マップを作成し，AC および MCSC に用いた．これは頭部 SPECT 検査での実用性を評価するためであった．均一な吸収マップを用いることにより，頭蓋骨部分での吸収・散乱を正確にモデリングできない．そのことが，画質や定量性に対して大きな劣化をもたらしたことは確認できなかったが，今後，トランスミッション CT を用いた場合と比較するなどして，その影響を調べる．

また，実際の臨床 SPECT 検査では，脳血流量診断や種々の神経受容体イメージング，さらには心筋領域においても交換神経機能のイメージング評価などを中心に，^{99m}Tc 標識薬剤だけでなく，^{123}I 標識薬剤が広く利用されている．とくに体内動態を数理解析することで生理機能を定量する分野では，^{123}I に対しても正確で定量的な再構成画像を提供する必要がある．一方 ^{123}I は 159 keV のメインピークガンマ線の他に高エネルギガンマ線も放出し，これがコリメータを突き抜けて画質を劣化させることが知られている〔19〕．今後，この septal penetration の影響を評価し，かつ補正法について検討していく．この septal penetration の影響が大きい場合の補正方法としては，コリメータ応答関数に septal penetration の成分を組み込む手法〔20〕や，septal penetration の成分をモンテカルロ法により推定する方法が挙げられる〔21〕．

6. おわりに

新しい SPECT 画像再構成法の頭部撮像に対する吸収補正と散乱線補正の妥当性が確認でき，空間解像度の補正の効果が大きな利点と考えられた．本手法は局所領域の定量評価などに有用であると考えられ，臨床 SPECT 検査の診断精度向上への貢献が期待される．

文　献

〔1〕 Zeng GL, Gullberg GT, Bai C et al: Iterative reconstruction of fluorine-18 SPECT using geometric point response correction. J Nucl Med **39**: 124-130, 1998

〔2〕 Fakhri GE, Buvat I, Benali H et al: Relative impact of scatter, collimator response, attenuation, and finite spatial resolution corrections in cardiac SPECT. J Nucl Med **41**: 1400-1408, 2000

〔3〕 Xiao J, de Wit TC, Staelens SG et al: Evaluation of 3D Monte Carlo-based scatter correction for ^{99m}Tc cardiac perfusion SPECT. J Nucl Med **47**: 1662-1669, 2006

〔4〕 Xiao J, de Wit TC, Zbijewski W et al: Evaluation of 3D Monte Carlo-based scatter correction for ^{201}Tl cardiac perfusion SPECT. J Nucl Med **48**: 637-644, 2007

〔5〕 Sohlberg A, Watabe H, Shidahara M et al: Body-contour versus circular orbit acquisition in cardiac SPECT: Assessment of defect detectability with channelized hotelling observer. Nucl Med Comm **28**: 937-942, 2007

〔6〕 Sohlberg A, Watabe H, Iida H: Acceleration of Monte Carlo-based scatter compensation for cardiac SPECT. Phys Med Biol **53**: 277-285, 2008

〔7〕 Hudson H, Larkin R: Accelerated image reconstruction using ordered subsets of projection data. IEEE Trans Med Imag **13**: 100-108, 1994

〔8〕 Di Bella EVR, Barclray AB, Eisner RL et al: A comparison of rotation-based methods for iterative reconstruction algorithms. IEEE Trans Nucl Sci **43**: 3370-3376, 1996

〔9〕 Metz CE, Atkins FB, Beck RN: The geometric transfer function component for scintillation camera collimators with straight parallel holes. Phys Med Biol **25**: 1059-1070, 1980

〔10〕 Zeng GL, Gullberg GT, Tsui BMW et al: 3-dimensional iterative reconstruction algorithms with attenuation and geometric point response correction. IEEE Trans Nucl Sci **38**: 693-702, 1991

[11] Yokoi T, Shinohara H, Onishi H: Performance evaluation of OSEM reconstruction algorithm incorporating three-dimensional distance-dependant resolution compensation for brain SPECT: A simulation study. Ann Nucl Med **16**: 11-18, 2002

[12] Iida H, Narita Y, Kado H et al: Effects of scatter and attenuation correction on quantitative assessment of regional cerebral blood flow with SPECT. J Nucl Med **39**: 181-189, 1998

[13] Shidahara M, Watabe H, Kim K et al: Impact of attenuation and scatter correction in SPECT for quantification of cerebral blood flow using 99mTc-Ethyl cystenate dimer. IEEE Trans Nucl Sci **49**: 5-11, 2002

[14] Woodcock E, Murphy T, Hemmings P et al: Techniques used in the GEM code for Monte Carlo neutronics calculations in reactors and other systems with complex geometry. Proc Conf. for applications of computing methods to reactor problems: 557, 1965

[15] Ljungberg M, Larsson A, Johansson L: A new collimator simulation in SIMIND based on the Delta-Scattering technique. IEEE Trans Nucl Sci **52**: 1370-1375, 2005

[16] de Jong HWAM, Slijpen ETP, Beekman FJ: Acceleration of Monte Carlo SPECT simulation using convolution-based forced detection. IEEE Trans Nucl Sci **48**: 58-64, 2001

[17] Kadrmas D, Frey E, Karimi S et al: Fast implementation of reconstruction-based scatter compensation in fully 3D SPECT image reconstruction. Phys Med Biol **43**: 857-873, 1998

[18] 飯田秀博，石田健二，今林悦子，他：灰白質領域の構造を模倣する立体ファントムの製作と評価．核医学 **46**(3): 284, 2009

[19] Muehllehner G, Luig H: Septal penetration in scintillation camera collimators. Phys Med Biol **18**: 855-862, 1973

[20] Chen J, Garcia EV, Galt JR et al: Improved quantification in ^{123}I cardiac SPECT imaging with deconvolution of septal penetration. Nucl Med Comm **27**: 551-558, 2006

[21] Staelens S, de Wit T, Beekman F: Fast hybrid SPECT simulation including efficient septal penetration modeling (SP-PSF). Phys Med Biol **52**: 3027-3043, 2007

Evaluation of the Quantitative Accuracy of a Novel Image Reconstruction Method with Monte Carlo-Based Scatter Compensation and Collimator Blurring Compensation for Brain SPECT

Tomonori SAKIMOTO[*1], Tsutomu ZENIYA[*2], Kenji ISHIDA[*3], Hiroshi WATABE[*2], Yoshiyuki HIRANO[*2], Antti SOHLBERG[*2], Kotaro MINATO[*1], Hidehiro IIDA[*2]

[*1] *Graduate School of Information Science, Nara Institute of Science and Technology*

[*2] *Department of Investigative Radiology, Advanced Medical Engineering Center, National Cardiovascular Center Research Institute*

[*3] *Molecular Imaging Labo Inc.*

The quality of SPECT images is degraded by collimator blurring, attenuation, and scatter. We have developed a new reconstruction method that includes attenuation compensation (AC), collimator-detector response compensation (CDRC), and Monte Carlo-based scatter compensation (MCSC). The aim of this study was to quantitatively evaluate our reconstruction method for brain SPECT in phantom experiments. We performed the following experiments using a SPECT gamma camera with an LEHR parallel-hole collimator (GCA-7200A, Toshiba, Japan): (1) measurement of spatial resolution using line sources, (2) measurement of uniformity in the reconstructed image of a cylindrical phantom filled with a uniform concentration of radioactivity, and (3) quantification of the concentration of radioactivity in a brain phantom. Resolution recovery significantly improved the resolution from 8.8 mm to 3.5 mm. The coefficient of variance (CoV) of the reconstructed image of the uniform cylindrical phantom was approximately 10%. The accuracy of quantification of the concentration of radioactivity was approximately 12%. These results suggest that our reconstruction algorithm with AC, MCSC, and CDRC is a valid method for improving resolution and quantitation in brain SPECT.

Key words: SPECT, Quantification, Scatter compensation, Monte Carlo, Collimator blurring compensation
Med Imag Tech **28** (2) : 135-144, 2010

﨑本智則（さきもと　とものり）

2008年新潟大学工学部福祉人間工学科卒業．同年，奈良先端科学技術大学院大学情報科学研究科入学．医用画像工学，生体計測に関する研究に従事．日本医用画像工学会，日本核医学会会員．

銭谷　勉（ぜにや　つとむ）

1991年山形大学工学部情報工学科卒業．1993年山形大学大学院工学研究科情報工学専攻修士課程修了．1993~1999年㈱日立メディコ勤務．2002年山形大学大学院理工学研究科システム情報工学専攻博士後期課程修了．博士（工学）．2001~2002年日本学術振興会特別研究員．2002年より国立循環器病センター研究所放射線医学部研究員．2008年奈良先端科学技術大学院大学情報科学研究科特任准教授．2009年より国立循環器病センター研究所先進医工学センター放射線医学部心血管撮影室室長．専門は医用画像工学．現在はSPECTイメージングの研究開発に従事．1998年日本医用画像工学会論文賞，2005年日本核医学会研究奨励賞，2008年米国核医学会若手研究者賞など受賞．

石田健二（いしだ　けんじ）

2006年新潟大学工学部福祉人間工学科卒業．2008年奈良先端科学技術大学院大学情報科学研究科修士課程修了，2008年㈱モレキュラーイメージングラボ入社，現在に至る．国立循環器病センター研究所放射線医学部の研修生として，SPECT画像定量化に関する研究に従事．

渡部浩司（わたべ　ひろし）

1995年東北大学大学院工学科卒業，博士（工学）．1993年英国ハマースミス病院，1997~1999年米国NIH PET部門に留学．1995~2009年国立循環器病センター研究所勤務．現在は，大阪大学大学院医学系研究科医薬分子イメージング学寄附講座准教授．専門は，PET/SPECTに関連したトレーサー動態解析，画像処理．

平野祥之（ひらの　よしゆき）

2008年大阪大学理学研究科卒業，博士（理学）．2008年国立循環器病センター研究所放射線医学部流動研究員として勤務．おもにPET, SPECTの定量化に関する研究に従事．

Antti Sohlberg（アンティ ソルベルグ）

2004年フィンランドクオピオ大学博士課程修了 Ph. D.．2005~2007年国立循環器病センター研究所先進医工学センター放射線医学部日本学術振興会外国人特別研究員，SPECT画像再構成の研究に従事．現在，スウェーデンHermes Medical Solutionsに勤務．

湊　小太郎（みなと　こたろう）

1970年京都大学工学部電気系学科卒業．1977年同大学院工学研究科（博）単位取得退学．1983年同大医学部附属病院放射線部助手．1983年同医療情報部助教授．1998年奈良先端科学技術大学院大学情報科学センター教授．2002年同大学院大学情報科学研究科（生命機能計測学講座）教授，現在に至る．京大工博．医療情報学，医用画像工学，生体計測などに関する研究に従事．日本医用画像工学会，日本生体医工学会，日本医療情報学会，電子情報通信学会，日本核医学会，IEEE，などの会員．

飯田秀博（いいだ　ひでひろ）

1984年筑波大学大学院博士課程物理学研究科修了．理学博士．秋田県立脳血管研究センター研究員，主任研究員を経て1999年より国立循環器病センター研究所・放射線医学部部長．その間，英国ハマースミス病院客員研究員，フィンランドトゥルク大学研究員，デンマークコペンハーゲン大学王立リス病院・客員教授．現在，奈良先端科学技術大学院大学連携大学院教授・大阪大学医学部連携大学院招聘教授を併任．専門はPET，SPECTイメージングの方法論の開発と臨床応用．

*　　*　　*

Radiol Phys Technol
DOI 10.1007/s12194-008-0038-x

Use of a clinical MRI scanner for preclinical research on rats

Akihide Yamamoto · Hiroshi Sato · Jun-ichiro Enmi · Kenji Ishida · Takayuki Ose · Atsuomi Kimura · Hideaki Fujiwara · Hiroshi Watabe · Takuya Hayashi · Hidehiro Iida

Received: 27 May 2008 / Revised: 22 August 2008 / Accepted: 27 August 2008

Abstract This study evaluated the feasibility of imaging rat brains using a human whole-body 3-T magnetic resonance imaging (MRI) scanner with specially developed transmit-and-receive radiofrequency coils. The T_1- and T_2-weighted images obtained showed reasonable contrast. Acquired contrast-free time-of-flight magnetic resonance angiography images clearly showed the cortical middle cerebral artery (MCA) branches, and interhemispheric differences could be observed. Dynamic susceptibility contrast MRI at 1.17 mm^3 voxel resolution, performed three times following administration of gadolinium diethylenetriamine pentaacetic acid (Gd-DTPA, 0.1 mmol/kg), demonstrated that the arterial input function (AIF) can be obtained from the MCA region, yielding cerebral blood flow (CBF), cerebral blood volume, and mean transit time (MTT) maps. The hypothalamus (HT) to parietal cortex (Pt) CBF ratio was 45.11 ± 2.85%, and the MTT was 1.29 ± 0.40 s in the Pt region and 2.32 ± 0.17 s in the HT region. A single dose of Gd-DTPA enabled the assessment of AIF within MCA territory and of quantitative CBF in rats.

Keywords Quantitative mapping · Human whole-body 3-T MRI scanner · Single dose of Gd-DTPA · Dynamic susceptibility contrast (DSC) · Preclinical research · Rat brain

A. Yamamoto · J. Enmi · K. Ishida · T. Ose · H. Watabe · T. Hayashi · H. Iida (✉)
Department of Investigative Radiology,
Advanced Medical Engineering Center,
National Cardiovascular Center Research Institute,
5-7-1, Fujishiro-dai, Suita, Osaka 565-8565, Japan
e-mail: iida@ri.ncvc.go.jp

A. Yamamoto · A. Kimura · H. Fujiwara · H. Watabe · T. Hayashi · H. Iida
Department of Medical Physics and Engineering,
Division of Health Sciences, Graduate School of Medicine,
Osaka University, 1-7, Yamada-oka, Suita,
Osaka 565-0871, Japan

H. Sato
Laboratory for Diagnostic Solution,
Advanced Medical Engineering Center,
National Cardiovascular Center Research Institute,
5-7-1, Fujishiro-dai, Suita, Osaka 565-8565, Japan

1 Introduction

Magnetic resonance imaging (MRI) has been widely used in preclinical research on experimental small animals. Studies have typically been aimed at understanding the pathophysiologic status and evaluating the efficacy/side effects of newly developed treatments, such as pharmaceutical and regenerative medicine. Recently, a different idea has surfaced: the use of a human whole-body MRI scanner for small-animal imaging [1]. Although small-animal-dedicated scanners are superior to clinical scanners in terms of providing a better signal-to-noise ratio, the available pulse sequences are different from those in clinical scanners, and the magnetic field strength is often much higher. Small-animal imaging with clinical scanners is important for directly addressing clinical questions and/or identifying the origins of signal changes, including various disease conditions in a clinical setting.

Smith et al. [2] demonstrated that anatomic brain T_1- weighted (T_1W) images and T_2-weighted (T_2W) images can be obtained for healthy rats by using a 1-T clinical MRI scanner with a specially designed radiofrequency (RF) coil, given a reasonable spatial resolution (0.1953 × 0.1953 × 2.5 mm, 24 min of T_1W and 48 min of T_2W). The image contrast was sufficiently high to

distinguish the cortical gray matter from the white matter [corpus callosum (CC)], as well as the lateral ventricle (LV) and interpeduncular cistern (IPC) from the thalamus (Thal). Guzman et al. [3] employed a clinical 1.5-T MRI scanner with a commercially available RF coil and demonstrated that both T_1W and T_2W images can be obtained with good contrast, a reasonable spatial resolution of 0.3125 × 0.3125 × 1.5 mm, and an acquisition time of 19 min 51 s, as well as 0.35156 × 0.375 × 1.5 mm at 8 min 34 s, corresponding to T_1W and T_2W images, respectively. Other investigators [4] applied a clinical 1.5-T MRI scanner with a 3-in.-diameter circular receive-only surface coil to assess anatomic images. Their images can be used to evaluate the pathophysiologic status of stroke [4] and cancer [5, 6], as well as the effects of neural excitotoxicity [3]. There were also several studies that used a clinical 3-T MRI scanner fitted with commercial and/or hand-made RF coils to investigate the pathophysiology of stroke [7, 8] and brain tumors in rats [6, 9, 10]. Generally speaking, anatomic images with better contrast can be obtained in a stronger magnetic field, although there are additional factors that may influence the signal-to-noise ratio (SNR) or spatial resolution of anatomic images. Contrast-free time-of-flight magnetic-resonance angiography (TOF-MRA) can also be performed on rats; a reasonable spatial resolution was obtained by using a clinical 3-T MRI scanner with a single-turn solenoid coil [11].

Dynamic susceptibility contrast MRI (DSC-MRI) [12] has been widely used in clinical diagnosis, particularly in patients with stroke [13–19] and tumors [20]. The application of clinical MRI scanners has been extended to DSC-MRI studies of small animals with stroke [21, 22] and tumors [23] using a 1.5-T MRI scanner. Up to now, small-animal studies have been performed on 1.5-T MRI scanners only, and 3-T scanners have not been employed so far. This is largely attributed to the fact that the susceptibility-induced inhomogeneous magnetic field can cause more serious distortion of the images at a higher static magnetic field. In DSC-MRI studies, the echo planar imaging (EPI) technique is mainly used because fast acquisition is required for accurate tracking of the bolus passage of MR contrast agents. The EPI technique, however, is very sensitive to magnetic field inhomogeneity, and thus the EPI images of small-animal brains may be severely distorted. The gradient slew rate (SR) is not high enough to support a sufficiently short echo spacing period when clinical scanners are used for high spatial resolution imaging of small objects. Moreover, injected materials may cause further distortion [24]. The degree of distortion of dynamic EPI images of small-animal brains produced by a 3-T clinical scanner is currently unknown. The arterial input function (AIF) is also questionable. To the best of our knowledge, no DSC-MRI studies of small-animal brains on 3-T clinical scanners have been reported.

This study attempted to evaluate the feasibility of developing a human whole-body 3-T MRI system for small animals, particularly DSC-MRI with a single dose of gadolinium-diethylenetriamine pentaacetic acid (Gd-DTPA). The quality of various images—including the anatomic T_1W images, T_2W images, time-of-flight magnetic resonance angiography (TOF-MRA) images and DSC images—was tested, and the availability of the AIF obtained from rat brain was evaluated.

2 Materials and methods

2.1 Subjects

The subjects were three healthy adult rats supplied by Japan SLC, Inc. (Shizuoka, Japan). All three rats were males, and they ranged in age from 20 to 24 weeks. Their weight range was between 400 and 600 g. Anesthesia was administered with an intramuscular injection of ketamine (33 mg/kg; Daiichi-Sankyo Co., Ltd., Tokyo, Japan) and xylazine (6.6 mg/kg; Bayer Yakuhin, Ltd., Osaka, Japan). The first rat (Sprague Dawley, SD) was used for T_1-W and T_2W imaging of the whole brain. The second rat, also a SD, was used for contrast-free TOF-MRA imaging. The third was a Wistar rat, which was used for a Gd-DTPA (0.1 mmol/kg; Bayer Yakuhin, Ltd., Osaka, Japan)-enhanced DSC-MRI sequence. Experiments were carried out according to the protocol approved by the Local Committee for Laboratory Animal Welfare, National Cardiovascular Center, Osaka, Japan.

2.2 MRI acquisition

A human whole-body 3-T MRI scanner (Signa, GE Healthcare, Milwaukee, WI, USA) equipped with a 55-cm bore was employed in this study. The gradient coil system was capable of providing a maximum gradient amplitude of 40 mT/m and an SR of 150 T m^{-1} s^{-1}. All sequence programs employed in this study were designed for clinical studies.

Two solenoid coils designed for rats were specially developed to cover the whole brain, and were capable of both transmitting and receiving RF pulses. The three-turn solenoid coil, which had a diameter of 42 mm and a length along its cylindrical axis of 18 mm, was attached to an apparatus made from an acrylic mold, as shown in Fig. 1. All components of the stereotaxic apparatus consisted of nonmagnetic materials that fixed the head positions of the rats during data acquisition. The RF coil was designed to have an impedance of 50 Ω at a resonance frequency of

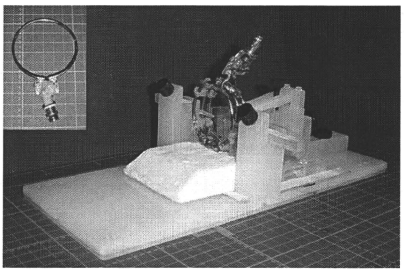

Fig. 1 The head fixation system for small animals, which was fitted with an MRI coil for RF transmission and reception. The coil is typically a three-turn solenoid; it can also be a single-turn coil, as shown on the *top left* of this figure

127.76 MHz. An additional single-turn surface coil of diameter 62 mm diameter was also developed for better homogeneity and was used for a single slice of DSC-MRI. The RF power in these coils had to be reduced to less than that used in the standard human head coil because of the diameter of the small coil. The transmission signal was therefore attenuated to 20 dB, which allowed the use of automated scanner software, including the calibration of the RF transmission power and receiver gains. All rats were fixed on the stereotaxic apparatus. They were placed at the center of the gantry and oriented with the craniocaudal axis perpendicular to the static magnetic field. Their heads were positioned inside the coil along the craniocaudal direction.

T_1W images were obtained with a conventional two-dimensional fast spin echo (2D-FSE) sequence. The repetition time (TR) was 1,500 ms [10]. The echo time (TE) was fixed at 14 ms. The echo train length (ETL) was 3. The field of view (FOV) was set at 40 × 30 mm^2, the slice thickness at 1.5 mm, the slice gap at 0.5 mm, the number of excitations (NEX) at 10, and the band width (BW) at 31.3 kHz. The acquired matrix (256 × 160) was interpolated, and null pixels were added in k-space to produce square matrices of 256 × 256. The acquisition time was 10 min 3 s.

T_2W images were obtained with a 2D-FSE and the following imaging parameters: TR, 4,100 ms; TE, 128 ms; ETL, 14; FOV, 40 × 30 mm; slice thickness, 1.5 mm; slice gap, 0.5 mm; NEX, 8; BW, 31.3 kHz; acquired matrix, 256 × 160, zero-filled to 256 × 256; phase direction, ventral-dorsal; acquisition time, 11 min 2 s.

Time-of-flight magnetic resonance angiography was performed using a three-dimensional flow-compensated spoiled gradient recalled (3D-SPGR) sequence prepared with magnetization transfer and with: TR, 53 ms; TE, 5.5 ms; flip angle (FA), 45°; BW, 16 kHz; FOV, 8 × 6 cm; slice thickness, 0.2 mm; one acquired slab of 512 × 512 × 64; voxel resolution, 0.156 × 0.156 × 0.2 mm^3; NEX, 1; acquisition time, 21 min 46 s.

Dynamic susceptibility contrast images were obtained following the intravenous administration of Gd-DTPA to the T_2*-weighted gradient echo dynamic images. A bolus of Gd-DTPA (0.1 mmol/kg) was injected manually into the tail vein with a 22-gauge catheter via 1 m of polyethylene tubing (PE50, internal diameter: 0.58 mm/outer diameter: 0.965 mm, Becton Dickinson and Company, Franklin Lakes, NJ, USA), and was followed by an additional administration of saline (1.0 ml). A multishot EPI (number of shots = 2) was employed to improve EPI distortion and temporal resolution. The imaging parameters were: TR, 142 ms; TE, 22.1 ms; FA, 20°; FOV, 40 × 40 mm; matrix size, 64 × 64, leading to a pixel size of 0.625 × 0.625 mm^2. The slice thickness was 3 mm in a single slice around the hypothalamus (HT). The temporal resolution was 0.284 s per image, and the acquisition time was 1 min 15 s. This assessment was repeated three times at intervals of 40 min and 10 min, corresponding to the first–second and second–third scans, respectively.

2.3 Data analysis

All MRI images were reconstructed on the same workstation provided for the GE Signa 3-T scanner used for the clinical programs. The images were then transferred to a Linux workstation. Lastly, data analysis was carried out using in-house and commercial software.

To evaluate the T_1W and T_2W image quality, we calculated the contrast-to-noise ratio (CNR) with an inter-tissue method [25–27] as follows: $CNR = (\pi/2)^{1/2} (SI_a - SI_b)/SI_{air}$, where SI_{air} represents the mean signal intensity of air, and SI_a and SI_b represent the signal intensities of tissue a and tissue b, respectively.

Angiograms were created by generating the partial maximum intensity projection (MIP) with commercial software [Virtual Place Liberty (VPL), AZE Co. Ltd., Tokyo, Japan]. Visible middle cerebral artery (MCA) branches and left-to-right differences in MCA were carefully investigated.

For the DSC images of slice sections containing the internal carotid artery (ICA) and/or MCA, a series of images were carefully observed. A region of interest (ROI) was carefully selected in the MCA region, from which the AIF was obtained, with the help of other anatomic information. To avoid susceptibility artifacts caused by air in the trachea, the area of the arterial circle of Willis was excluded from the definition of the AIF. The anterior cerebral artery was also excluded because of possible susceptibility effects attributed to venous blood. A Gaussian filter of full width at half maximum (FWHM) 1.1 mm

was applied to all dynamic images. The time versus signal intensity curves (TICs) were converted to the Gd-DTPA concentration according to Eq. 1 given in the "Appendix." Functional mapping images of the mean transit time (MTT), cerebral blood volume (CBV), and cerebral blood flow (CBF) were carried out with the deconvolution method [28]. The theory behind this is described in detail in the "Appendix." For ROI analysis, images of matrix size 64 × 64 were converted to 256 × 256 using a sinc interpolation function.

3 Results

T_1W and T_2W images reconstructed with a spatial resolution of 0.156 × 0.188 × 1.5 mm are shown in Fig. 2. White matter could be discriminated from cortical and deep gray matter regions. The locations of small anatomic features such as the caudate putamen (CPu), striatum, the CC, and the hippocampus (HC) could also be identified in both T_1W and T_2W anatomic images. The CNRs between the HC and CC were 15.6 and 9.8, respectively, for the T_1W and T_2W images shown in Fig. 2. The CNRs between the HC and IC were 23.2 and 13.6, respectively, although the CNR may be underestimated due to the contamination of signal from the globus pallidus.

Results for MIP images obtained with contrast-free TOF-MRA are shown in Fig. 3. Coronal MIP images around the HT of thickness 5 mm are shown in Fig. 3a. In this figure, the slice section contained ICAs and MCA. The MCA, the cortical branches in both the left and right hemispheres, can be identified. It is important to note that the anatomic structure of the cortical MCA arteries is different between the right and left hemispheres. The ROI for the AIF was selected in the MCA region and is shown by the arrows in Fig. 3a and b.

A typical example of a DSC-MRI image is shown in Fig. 4. Distortion of the DSC-MRI images is visible in Fig. 4A in the phase direction. A magnified area from dynamic images of the MCA region (shown as a rectangle in Fig. 4A) is displayed in Fig. 4B. Several pixels indicate temporal changes in pixel contrast as a function of time, and these are reflected by Gd-DTPA negative enhancement. The pixel signal intensity varied as shown in Fig. 4C, and the curve shown was employed to estimate the AIF. Figure 5 shows the TIC in this area together with the TIC for the whole brain region obtained from each of the three scans. The curves were visually reproducible in terms of the shapes, heights and widths of the curves around the peak, as well as the tail height at the end of the scan. It should also be noted that the baseline was consistent before each injection of Gd-DTPA, even though the second and

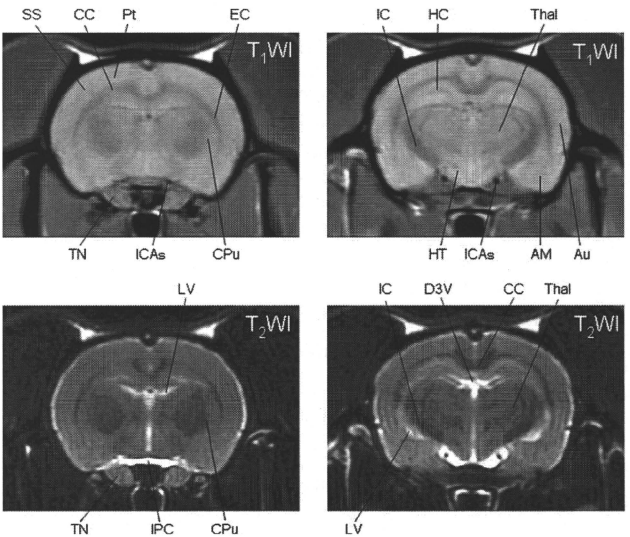

Fig. 2 T_1W images (*top*) and T_2W images (*bottom*) obtained from an SD rat, with the following anatomic locations as indicated: the somatosensory cortex (*SS*), corpus callosum (*CC*), parietal cortex (*Pt*), external capsule (*EC*), caudate putamen (*CPu*), internal capsule (*IC*), hippocampus (*HC*), thalamus (*Thal*), auditory cortex (*Au*), amygdala (*AM*), hypothalamus (*HT*), internal carotid arterial system (*ICAs*), trigeminal nerve (*TN*), interpeduncular cistern (*IPC*), dorsal third ventricle (*D3V*), and the lateral ventricle (*LV*). These slice sections were located −1.5 mm (*left*) and −3.5 mm (*right*), respectively, from the bregma

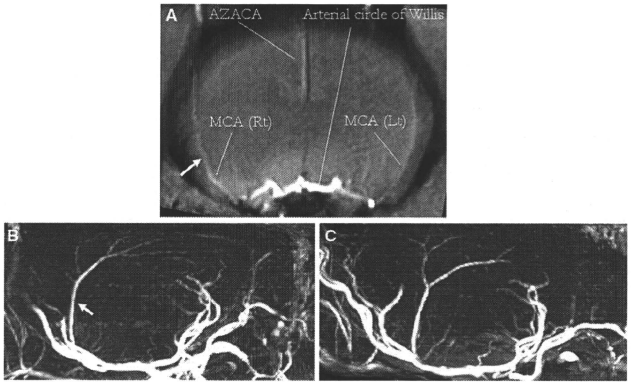

Fig. 3 Partial maximum intensity projection maps of contrast-free time-of-flight MRA obtained for a Sprague Dawley rat. Maps represent areas around the Thal (**a**), right hemisphere (**b**), and left hemisphere (**c**). The *white arrows* indicate the selected ROI level (as described in the "Discussion"). *AZACA*, azygos anterior cerebral artery

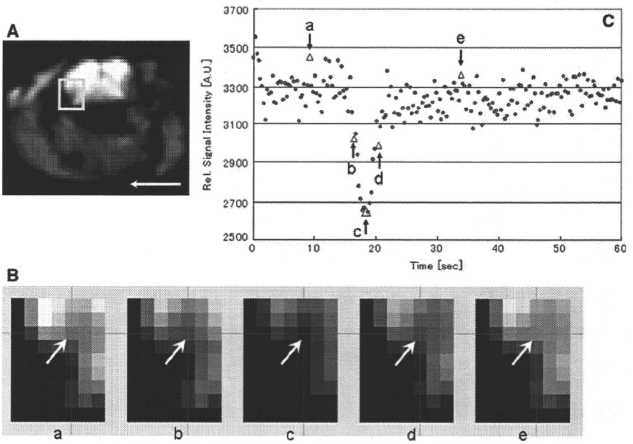

Fig. 4 Typical time-frame images obtained from Gd-bolus tracking T_2*-weighted dynamic images (after the first injection). A *white rectangle* was placed in the MCA area (**a**), and magnified images of this rectangle were visualized as *a*, *b*, *c*, *d*, and *e* in **b**. The TIC within the pixels is indicated by *white arrows* in **b**. The data were then plotted in a graph (**c**). Typical data points were extracted from the first injection at the times of 9.2 (*a*), 16.4 (*b*), 18.1 (*c*), 20.1 (*d*), and 33.9 (*e*) s. The phase direction is shown as a *white arrow* in **a**

the third curves should have been affected by the previous injection of Gd-DTPA.

Functional mapping images of CBF, CBV, and MTT calculated according to the theory described in the "Appendix" are shown in Fig. 6. Images obtained from this sequential assessment appeared to be reasonably clear, although slightly noisy, and were consistent among the scans. The absolute CBFs (mean ± SD) in the cortical gray matter area (mainly the parietal cortex, Pt) were 24.04 ± 2.88, 17.75 ± 3.34, and 31.87 ± 7.27 ml g^{-1} min^{-1} for the first, second, and third scans, respectively. The HT-to-Pt CBF ratios were 46.7, 51.5, and 43.0% for the first, second, and third scans, respectively. The CBVs were 0.49 (0.44), 0.50 (0.35), and 0.47 (0.41) ml/ml in the Pt (the HT) region in the first, second, and third scans, respectively. The MTTs in the same regions were 1.22 (2.51), 1.72 (2.29),

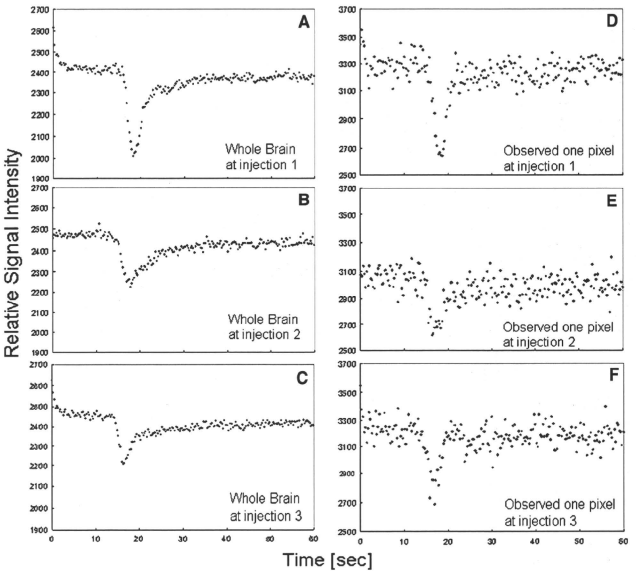

Fig. 5 TIC dynamic changes in the whole brain are shown in the first injection (**a**), the second injection (**b**), and the third injection (**c**). For each injection, a one-pixel ROI was selected and observed, as shown for the first (**d**), second (**e**) and third (**f**) injections, respectively. The negative enhancement changes in the rate from peak signal intensity to baseline were 16.8% (**a**), 10.0% (**b**), and 10.3% (**c**) at the whole brain (average 12.3, SD 3.9). The peak-to-base fractions at selected ROIs were 19.2% (**d**), 14.5% (**e**), and 16.9% (**f**) (average 16.9, SD 2.3), for the first, second, and third injections, respectively

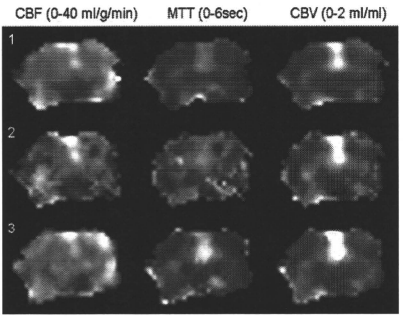

Fig. 6 *First column on the left*: CBF maps using the AIF from MCA, pictured in a grayscale from 0 to 4 ml g^{-1} min^{-1}. MTT maps are shown in the *middle column*, followed by CBV maps of 0–2 ml g^{-1} min^{-1} in the *column on the right*. Deconvolution was carried out pixel by pixel with b-SVD and then smoothed to 0.15625 × 0.15625 mm in-plane resolution from the acquired voxel resolution of 0.625 × 0.625 × 3 mm (1.17 mm^3) in DSC-MRI

and 0.92 (2.16) s in each of the three scans. Among the three injections, the absolute MTTs (mean ± SD) were 1.29 ± 0.40 s in the Pt and 2.32 ± 0.17 s in the HT region.

4 Discussion

This study demonstrated that our system of a human whole-body 3-T MRI fitted with an in-house solenoid coil developed for small animals can provide morphologic and functional images of the rat brain in vivo. The quality of T_1W and T_2W images obtained with a scan duration of approximately 10 min was better than those obtained in previous studies in which 1.5-T clinical MRI scanners [3] were employed. The neocortex and large subcortical structures, such as the Thal and HC, are readily recognized from their topographic relationship to the CC, the ventricular system, and the subarachnoid space [2]. In T_1W images, the cerebrospinal fluid (CSF)-containing spaces are visible as they are hypointense, and the arterial flow showed a signal loss caused by so-called flow void effects, which is typically seen in the spin echo sequence [2]. In T_2W images, the CSF was bright and white (prolonged T_2 relaxation time), whereas the myelinated white matter was black (short T_2 relaxation time). The white matter tracts such as the IC and CC were clearly visible in both T_1W and T_2W images, and better quality was obtained compared to previous reports employing 1.0- and 1.5-T clinical MRI scanners [2, 3].

Magnetic resonance angiography images also clearly showed the structure of the distal MCA branches. The MRA findings of interhemispheric differences with regards to MCA in the SD rat were also consistent with a previous report on Wistar rats [29], which indicated left-to-right asymmetric structure in three out of ten Wistar rats using a 7-T MRI scanner dedicated to small-animal imaging [29]. Our MRA images are superior to those obtained in previous work [11] that employed a clinical 3-T MRI scanner and that only showed the major cerebral arteries and the carotid arteries because they focused mainly on validating occlusion models [11]. The superior quality of our MRA images can largely be attributed to the type of RF coil we used. Ours is a three-turn solenoid coil that covers only the cerebral area, whereas the previous work [11] employed a single-turn coil (diameter of 6.4 cm and length of 10 cm) that covered the whole head, including the brain and the neck. Additionally, the prolonged acquisition period in our study (almost 20 min) compared to the acquisition period used in the previous study [11] (almost 4 min) may have been a factor that led to higher-quality MRA images.

An important point about this study is that DSC-MRI images of reasonable quality can also be obtained with a clinical MRI scanner at 3 T on rats. In addition, we were able to extract the AIF from the rat brain, which is an important accomplishment. Selection of an ROI in the MCA region successfully provided the AIF. Spatial distortion or susceptibility artifacts were not visible in our observations. Signal changes were obtained during DSC-MRI following a single dose of Gd-DTPA. During this study, the dedicated transmit and receive RF coils were considered to be crucial to obtaining a reasonable SNR. Our study was performed with the same sequence and the same dose rate (0.1 mmol/kg) of Gd-DTPA that are commonly used in clinical examinations. Moreover, it was performed with high ($1.17\ mm^3$)-resolution dynamic imaging.

The quantitative images of CBF were consistent with those in a previous report on the use of [^{14}C] iodoantipyrine [30]. Namely, the HT-to-Pt contrast in CBF was 43–52% in this study, which is close to the values reported by Bloom et al. [30] of 44–58%. Although the absolute CBF and CBV values in our study were different from those obtained previously [13, 30, 31], the uncertain scaling factors for each of these were canceled out when calculating the MTT with Eq. 5 [32] (see also the "Appendix"). The MTT obtained in this study was comparable to those obtained in previous work [31, 33].

We noticed that the absolute CBF and CBV values were overestimated, which suggests that some limitations apply, such as the partial volume effect (PVE) caused by insufficient spatial resolution as compared with the anatomic structure of the MCA. Detection of AIF with a repeat injection was performed (Fig. 5, right row). The major MCA diameter was approximately 0.5 mm at the maximum, as evaluated from Fig. 3, which suggested that the measured AIF is largely influenced by the PVE [24]. Also, the differences in absolute value may be due to the fact that a nonlinear relationship exists between the signal intensity and the contrast agent concentration. Previous reports have proposed nonlinearity correction methods for brain tissue [34] and AIF [35]. Further studies are needed to confirm the accuracy and the reproducibility [36]. Image distortion caused by dielectric effects [37] and/or EPI distortion [38] are other sources of error, and should be investigated systematically.

Improving the quality of the original dynamic images acquired would also improve the mapping image quality. In order to achieve better detection of the dynamic susceptibility contrast caused by T_2* signals, the optimization of TE, FA and the acquisition matrix should be investigated. We speculate that a multichannel phased array coil and parallel imaging techniques would reduce the level of distortion. The DSC-MRI in this study was obtained for only a single slice. Further careful attention is needed to perform multislice imaging in order to minimize inflow effects [35]. In our study, the contrast concentration $C(t)$ curves including the AIFs varied slightly among the three injections. A sophisticated injector system that is MR-compatible may improve the variation.

A dedicated high magnetic field scanner equipped with a dedicated small bore is the optimal device for small-animal imaging. However, such systems are not commonly available. The system developed in this study might serve as a low-cost solution or an alternative. The use of the present system provides an opportunity to use the same imaging platform available for clinical studies for small-animal imaging [7]. This would allow us to determine pathophysiological status from MRI signals using animal models with various diseases. More importantly, the optimization of several scan parameters, which has been difficult to achieve in clinical patients, can easily be performed on small animals with this system. In particular, the reproducibility of the assessment of CBF with DSC-MRI, which has been reported to be a limitation on clinical studies [19, 36], could be improved by performing a systematic evaluation of each scan parameter when this system is used on small animals rather than clinical patients. With the addition of a high-strength insert gradient coil [39], which allows for thinner slices and much faster read-out, the system performance and the spatial resolution with an acceptable SNR can be improved. The use of adapting coils could be an effective solution for those who operate MR scanners for human subjects and intend to gain experience [40] in preclinical research.

5 Conclusion

In this preclinical study on rats, reasonable image quality was obtained for T_1W, T_2W, and contrast-free TOF-MRA images generated using a human whole-body 3-T MRI scanner and a newly developed solenoid coil. In DSC-MRI, this system visualized transient signal changes with a single dose of Gd-DTPA and using the same sequences commonly used in clinical examinations. A human whole-body 3-T MRI scanner and dedicated coil make it possible to detect the AIF in the MCA region of Wistar rats. High-resolution DSC-MRI was accomplished with a clinical scanner, but the spatial resolution with an acceptable SNR was insufficient for the rat brain. Although there may be some remaining issues relating to AIF, we have shown the potential of DSC-MRI in our study.

Acknowledgments The authors would like to express our appreciation to the reviewers, the editors and the editorial assistants of *Radiological Physics and Technology* for their invaluable advice on how to improve our manuscript. This study was supported by a grant for research on Advanced Medical Technology from the Ministry of Health, Labor and Welfare, Japan. We would like to thank the VPL released by AZE Ltd. (Tokyo, Japan) and the software library provided by the Oxford University Center for Functional MRI of the Brain. We are grateful to the staff at the National Cardiovascular Center for their invaluable contributions and efforts. Last but not least, we would like to express our thanks to Miss Atra Ardekani (a summer intern from McGill University in Montreal, Quebec, Canada).

Appendix: Calculation of functional mapping images from DSC-MRI

The observed TIC $S(t)$ was converted to a time-versus-concentration curve (TCC) $C(t)$ by the following equation [16, 36]:

$$C(t) = k \cdot \Delta R2^*(t) = -k \cdot \ln(S(0)/S(t))/\mathrm{TE}, \quad (1)$$

where $\Delta R2^*$ is the change in the T_2^* relaxation rate and k is a constant. In this study, it was assumed that $k = 1$. $S(0)$ is the pre-contrast (baseline) signal and $S(t)$ is the measured signal at time t. The next step was to fit this first-pass period of TCC to a gamma variate function:

$$C(t) = a(t-b)^c \exp(-(t-b)/d), \quad (2)$$

where a, b, c, and d were determined by nonlinear least-squares fitting. To minimize the effects of the recirculation of the contrast agent, data were neglected in the fit if these concentrations were less than 50% of the maximum after the peak of the TCC.

The fitted tissue TCC $Ct(t)$ was deconvolved by the fitted AIF $C_{\mathrm{AIF}}(t)$ by using singular value decomposition with a block-circulant deconvolution matrix (b-SVD) method [28] according to the equation

$$\mathrm{CBF} \cdot R(t) = Ct(t) \otimes^{-1} C_{\mathrm{AIF}}(t), \quad (3)$$

where $\otimes^{-1}$ represents the deconvolution operator and $R(t)$ is a residue function representing the tissue response to an instantaneous bolus. $\mathrm{CBF} \cdot R(t)$ was estimated by deconvolving $Ct(t)$ by $C_{\mathrm{AIF}}(t)$ using b-SVD, and then CBF was determined as the maximum value of the obtained $\mathrm{CBF} \cdot R(t)$.

The CBV was calculated as follows:

$$\mathrm{CBV} = \int_0^\infty Ct(t)\mathrm{d}t \Big/ \int_0^\infty C_{\mathrm{AIF}}(t)\mathrm{d}t. \quad (4)$$

Lastly, the MTT is calculated from CBF and CBV by applying the central volume principle [32]:

$$\mathrm{MTT} = \mathrm{CBV}/\mathrm{CBF}. \quad (5)$$

References

1. Brockmann MA, Kemmling A, Groden C. Current issues and perspectives in small rodent magnetic resonance imaging using clinical MRI scanners. Methods. 2007;43:79–87.
2. Smith DA, Clarke LP, Fiedler JA, Murtagh FR, Bonaroti EA, Sengstock GJ, et al. Use of a clinical MR scanner for imaging the rat brain. Brain Res Bull. 1993;31(1–2):115–20.
3. Guzman R, Lövblad KO, Meyer M, Spenger C, Schroth G, Widmer HR. Imaging the rat brain on a 1.5 T clinical MR-scanner. J Neurosci Methods. 2000;97(1):77–85.
4. Fujioka M, Taoka T, Matsuo Y, Hiramatsu KI, Sakaki T. Novel brain ischemic change on MRI: delayed ischemic hyperintensity on T_1-weighted images and selective neuronal death in the caudoputamen of rats after brief focal ischemia. Stroke. 1999;30(5):1043–6.
5. Thorsen F, Ersland L, Nordli H, Enger PO, Huszthy PC, Lundervold A, et al. Imaging of experimental rat gliomas using a clinical MR scanner. J Neurooncol. 2003;63(3):225–31.
6. Biswas J, Nelson CB, Runge VM, Wintersperger BJ, Baumann SS, Jackson CB, et al. Brain tumor enhancement in magnetic resonance iimaging: comparison of signal-to-noise ratio (SNR) and contrast-to-noise ratio (CNR) at 1.5 versus 3 Tesla. Invest Radiol. 2005;40:792–7.
7. Shimamura M, Sato N, Sata M, Kurinami H, Takeuchi D, Wakayama K, et al. Delayed postischemic treatment with fluvastatin improved cognitive impairment after stroke in rats. Stroke. 2007;38:3251–8.
8. Lee JM, Zhai G, Liu Q, Gonzales ER, Yin K, Yan P, et al. Vascular permeability precedes spontaneous intracerebral hemorrhage in stroke-prone spontaneously hypertensive rats. Stroke. 2007;38:3289–91.
9. Wintersperger BJ, Runge VM, Biswas J, Reiser MF, Schoenberg SO. Brain tumor enhancement in mr imaging at 3 Tesla: comparison of SNR and CNR gain using TSE and GRE techniques. Invest Radiol. 2007;42:558–63.
10. Sato H, Enmi J, Teramoto N, Hayashi T, Yamamoto A, Tsuji T, et al. Comparison of Gd-DTPA-induced signal enhancements in rat brain C6 glioma among different pulse sequences in 3-Tesla magnetic resonance imaging. Acta Radiol. 2008;49:172–9.
11. Yang YM, Feng X, Yao ZW, Tang WJ, Liu HQ, Zhang L. Magnetic resonance angiography of carotid and cerebral arterial

occlusion in rats using a clinical scanner. J Neurosci Methods. 2008;167(2):176–83.
12. Rosen BR, Belliveau JW, Vevea JM, Brady TJ. Perfusion imaging with NMR contrast agents. Magn Reson Med. 1990;14(2):249–65.
13. Calamante F, Thomas DL, Pell GS, Wiersma J, Turner R. Measuring cerebral blood flow using magnetic resonance imaging techniques. J Cereb Blood Flow Metab. 1999;19(7):701–35.
14. Yamada K, Wu O, Gonzalez RG, Bakker D, Østergaard L, Copen WA, et al. Magnetic resonance perfusion-weighted imaging of acute cerebral infarction: effect of the calculation methods and underlying vasculopathy. Stroke. 2002;33(1):87–94.
15. Tamura H, Hatazawa J, Toyoshima H, Shimosegawa E, Okudera T. Detection of deoxygenation-related signal change in acute Ischemic stroke patients by T2*-weighted magnetic resonance imaging. Stroke. 2002;33(4):967–71.
16. Calamante F, Gadian DG, Connelly A. Quantification of perfusion using bolus tracking magnetic resonance imaging in stroke: assumptions, limitations, and potential implications for clinical use. Stroke. 2002;33(4):1146–51.
17. Latchaw RE, Yonas H, Hunter GJ, Yuh WT, Ueda T, Sorensen AG, et al. Guidelines and recommendations for perfusion imaging in cerebral ischemia: a scientific statement for healthcare professionals by the Writing Group on Perfusion Imaging, from the Council on Cardiovascular Radiology of the American Heart Association. Stroke. 2003;34(4):1084–104.
18. Carroll TJ, Rowley HA, Haughton VM. Automatic calculation of the arterial input function for cerebral perfusion imaging with MR imaging. Radiology. 2003;227(2):593–600.
19. Wintermark M, Sesay M, Barbier E, Borbély K, Dillon WP, Eastwood JD, et al. Comparative overview of brain perfusion imaging techniques. Stroke. 2005;36(9):83–99.
20. Bruening R, Kwong KK, Vevea MJ, Hochberg FH, Cher L, Harsh GR 4th, et al. Echo-planar MR determination of relative cerebral blood volume in human brain tumors: T1 versus T2 weighting. AJNR Am J Neuroradiol. 1996;17(5):831–40.
21. Chen F, Suzuki Y, Nagai N, Peeters R, Coenegrachts K, Coudyzer W, et al. Visualization of stroke with clinical MR imagers in rats: a feasibility study. Radiology. 2004;233:905–11.
22. Chen F, Suzuki Y, Nagai N, Sun X, Coudyzer W, Yu J, et al. Delayed perfusion phenomenon in a rat stroke model at 1.5 T MR: An imaging sign parallel to spontaneous reperfusion and ischemic penumbra? Eur J Radiol. 2007;61:70–8.
23. Fan G, Zang P, Jing F, Wu Z, Guo Q. Usefulness of diffusion/perfusion-weighted MRI in rat gliomas: correlation with histopathology. Acad Radiol. 2005;12(5):640–51.
24. van Osch MJ, van der Grond J, Bakker CJ. Partial volume effects on arterial input functions: shape and amplitude distortions and their correction. J Magn Reson Imaging. 2005;22(6):704–9.
25. Wada Y, Hara T, Miyati T. Basic assessment of the CNR measurement method of MRI system in phantom—suggestion for improvement in the CNR evaluation method. Nippon Hoshasen Gijutsu Gakkai Zasshi. 2008;64(2):268–76.
26. Ogura A, Maeda F, Miyai A, Hongoh T. Accuracy of contrast-to-noise ratio measurement for magnetic resonance clinical images. Nippon Hoshasen Gijutsu Gakkai Zasshi. 2004;60(11):1543–9.
27. Miyati T. Image quality assessment in magnetic resonance imaging. Nippon Hoshasen Gijutsu Gakkai Zasshi. 2002;58(1):40–8.
28. Wu O, Ostergaard L, Weisskoff RM, Benner T, Rosen BR, Sorensen AG. Tracer arrival timing-insensitive technique for estimating flow in MR perfusion-weighted imaging using singular value decomposition with a block-circulant deconvolution matrix. Magn Reson Med. 2003;50:164–74.
29. Besselmann M, Liu M, Diedenhofen M, Franke C, Hoehn M. MR angiographic investigation of transient focal cerebral ischemia in rat. NMR Biomed. 2001;14(5):289–96.
30. Bloom AS, Tershner S, Fuller SA, Stein EA. Cannabinoid-induced alterations in regional cerebral blood flow in the rat. Pharmacol Biochem Behav. 1997;57(4):625–31.
31. Shockley RP, LaManna JC. Determination of rat cerebral cortical blood volume changes by capillary mean transit time analysis during hypoxia, hypercapnia and hyperventilation. Brain Res. 1998;454(1–2):170–8.
32. Meier P, Zierler KL. On the theory of the indicator-dilution method for measurement of blood flow and volume. J Appl Physiol. 1954;6:731–44.
33. Johansson E, Månsson S, Wirestam R, Svensson J, Petersson JS, Golman K, et al. Cerebral perfusion assessment by bolus tracking using hyperpolarized 13C. Magn Reson Med. 2004;51(3):464–72.
34. Enmi J, Hayashi T, Watabe H, Moriwaki H, Yamada N, Iida H. Measurement of cerebral blood flow with dynamic susceptibility contrast MRI and comparison with O-15 positron emission tomography. Int Congr Ser. 2004;1265:150–8.
35. Calamante F, Vonken EJ, van Osch MJ. Contrast agent concentration measurements affecting quantification of bolus-tracking perfusion MRI. Magn Reson Med. 2007;58:544–53.
36. Grandin CB, Bol A, Smith AM, Michel C, Cosnard G. Absolute CBF and CBV measurements by MRI bolus tracking before and after acetazolamide challenge: repeatability and comparison with PET in humans. Neuroimage. 2005;26:525–35.
37. Kuhl CK, Träber F, Schild HH. Whole-body high-field-strength (3.0-T) MR imaging in clinical practice. Part I. Technical considerations and clinical applications. Radiology. 2008;246(3):675–96.
38. Jezzard P, Clare S. Sources of distortion in functional MRI data. Hum Brain Mapp. 1999;8(2–3):80–5.
39. Mayer D, Zahr NM, Adalsteinsson E, Rutt B, Sullivan EV, Pfefferbaum A. In vivo fiber tracking in the rat brain on a clinical 3T MRI system using a high strength insert gradient coil. Neuroimage. 2007;35(3):1077–85.
40. Graf H, Martirosian P, Schick F, Grieser M, Bellemann ME. Inductively coupled rf coils for examinations of small animals and objects in standard whole-body MR scanners. Med Phys. 2003;30(6):1241–5.

Journal of Cerebral Blood Flow & Metabolism (2009) 29, 355–364

www.jcbfm.com

A physiologic model for recirculation water correction in $CMRO_2$ assessment with $^{15}O_2$ inhalation PET

Nobuyuki Kudomi, Takuya Hayashi, Hiroshi Watabe, Noboru Teramoto, Rishu Piao, Takayuki Ose, Kazuhiro Koshino, Youichirou Ohta and Hidehiro Iida

Department of Investigative Radiology, Advanced Medical-Engineering Center, National Cardiovascular Center Research Institute, Osaka, Japan

Cerebral metabolic rate of oxygen ($CMRO_2$) can be assessed quantitatively using $^{15}O_2$ and positron emission tomography. Determining the arterial input function is considered critical with regards to the separation of the metabolic product of $^{15}O_2$ (RW) from a measured whole blood. A mathematical formula based on physiologic model has been proposed to predict RW. This study was intended to verify the adequacy of that model and a simplified procedure applying that model for wide range of species and physiologic conditions. The formula consists of four parameters, including of a production rate of RW (*k*) corresponding to the total body oxidative metabolism ($BMRO_2$). Experiments were performed on 6 monkeys, 3 pigs, 12 rats, and 231 clinical patients, among which the monkeys were studied at varied physiologic conditions. The formula reproduced the observed RW. Greater *k* values were observed in smaller animals, whereas other parameters did not differ amongst species. The simulation showed $CMRO_2$ sensitive only to *k*, but not to others, suggesting that validity of determination of only *k* from a single blood sample. Also, *k* was correlated with $BMRO_2$, suggesting that *k* can be determined from $BMRO_2$. The present model and simplified procedure can be used to assess $CMRO_2$ for a wide range of conditions and species.
Journal of Cerebral Blood Flow & Metabolism (2009) **29,** 355–364; doi:10.1038/jcbfm.2008.132; published online 5 November 2008

Keywords: arterial input; $CMRO_2$; mathematical modeling; recirculation water; PET

Introduction

Cerebral metabolic rate of oxygen ($CMRO_2$) can be quantitatively assessed using ^{15}O-labeled oxygen ($^{15}O_2$) and positron emission tomography (PET). This technique is based on an estimation of influx rate of $^{15}O_2$ to the cerebral tissue from arterial blood. Using information of cerebral blood flow (CBF) that may be obtained either from a separate scan with ^{15}O-labeled water ($H_2^{15}O$) or from the clearance rate $^{15}O_2$ of tissue, the oxygen extraction fraction (OEF) can also be calculated. The arterial input function must be determined before beginning this calculation. More specifically, a metabolic product of $^{15}O_2$ in the arterial blood, as a form of ^{15}O-labeled water (i.e., recirculating ^{15}O-water or RW) needs to be accurately estimated.

The arterial whole blood radioactivity curve can be obtained by measuring the radioactivity concentration of continuously withdrawn whole blood using a monitoring device (Eriksson *et al*, 1988; Eriksson and Kanno, 1991; Votaw and Shulman, 1998; Kudomi *et al*, 2003). Assessment of a time-dependent RW curve may be achieved by separating the plasma from the whole blood samples. This, however, requires labor-intensive procedures of frequent, manual arterial blood samplings, the centrifugation of all collected blood samples, and radioactivity measurements for both whole blood and plasma (Holden *et al*, 1988).

Ohta *et al* (1992) proposed to neglect the component of RW from the arterial input function. This technique fits three parameters of $CMRO_2$, CBF, and

Correspondence: Dr H Iida, Department of Investigative Radiology, Advanced Medical-Engineering Center, National Cardiovascular Center Research Institute, 5-7-1, Fujishirodai, Suita, Osaka 565-8565, Japan.
E-mail: iida@ri.ncvc.go.jp
This study was supported by the Program for Promotion of Fundamental Studies in Health Science of the Organization for Pharmaceutical Safety and Research of Japan, a Grant for Research on Advanced Medical Technology from the Ministry of Health, Labour and Welfare (MHLW), Japan, and by Nakatani Electronic Measuring Technology Association of Japan (NK).
Received 2 May 2005; revised 6 October 2008; accepted 11 October 2008; published online 5 November 2008

cerebral blood volume (CBV) to the kinetic $^{15}O_2$ data obtained from a single PET scan after the bolus administration of $^{15}O_2$. To minimize errors which result from neglecting RW, only the initial 3 mins of data after the bolus inhalation of $^{15}O_2$ were used when calculating the parameters. This approach has been applied to evaluate the magnitude of increase in $CMRO_2$ relative to that in CBF during cognitive stimulation tasks (Fujita *et al*, 1999; Vafaee and Gjedde, 2000; Okazawa *et al*, 2001*a*, *b*; Yamauchi *et al*, 2003; Mintun *et al*, 2002), but one of the drawbacks to this technique is the lack of accurate statistics, which is due to the use of a short scan duration.

Iida *et al* (1993) have developed a mathematical formula to predict the production of RW based on a physiologic model, which allows prolongation of the PET acquisition period with an additional statistical accuracy. The formula assumes a fixed rate constant for production of RW from $^{15}O_2$ in the body. This is based on the fact that the observed rate constant did not vary among clinical subjects, and thus causes nonsignificant errors in $CMRO_2$. However, the study is limited only to human subjects studied at rest, and results have not been verified using other species such as rat and mouse (Magata *et al*, 2003; Temma *et al*, 2006; Yee *et al*, 2006). Also, the findings have not been evaluated on humans who are under physiologic stress, though under such conditions the whole-body oxygen consumption is expected to change. Moreover, it is important to extend the approach to physiologically stressed conditions as recent progress for assessing $CMRO_2$ and CBF simultaneously from a short period dynamic scan by using a dual tracer autoradiography (DARG) (Kudomi *et al*, 2005). The DARG has enabled the $^{15}O_2$ PET to assess $CMRO_2$ and CBF simultaneously at various physiologically activated conditions.

The aim of this study is to verify the method used to estimate the arterial RW during the $^{15}O_2$ inhalation for simultaneous determination of $CMRO_2$ and CBF from the rapid procedures of $^{15}O_2$ PET. The feasibility of a simplified procedure is also being investigated. Applicability of this approach was tested for a wide range of species under various physiologic conditions. Experiments were designed to apply for different species as well as different physiologic conditions. A simulation study was also performed to evaluate the level of error sensitivity associated with this approach.

Materials and methods

Theory

Variables used in the recirculating water model are summarized in Table 1. The mathematical model that formulates the time-dependent RW in arterial blood consists of three rate constants: (1) the production rate of RW or k (per min), proportional to oxidative metabolism in the total body system ($BMRO_2$), (2) the forward diffusion rate (k_w, per min) of the metabolized ^{15}O-water between the blood and interstitial spaces in the body, and (3) the backward diffusion rate (k_2, per min) of the metabolized ^{15}O-water between the blood and interstitial spaces in the body. The differential equations for the arterial activity concentration of ^{15}O-water at a time t (secs) ($A_w(t)$, Bq/mL), after the physical decay correction can be expressed as follows (Huang *et al*, 1991):

$$\frac{d}{dt}A_w(t) = k \cdot A_o(t) - k_w \cdot A_w(t) + k_2 \cdot C(t) \quad (1a)$$

$$\frac{d}{dt}C(t) = k_w \cdot A_w(t) - k_2 \cdot C(t) \quad (1b)$$

$$A_t(t) = A_o(t) + A_w(t) \quad (1c)$$

where $A_o(t)$ and $A_t(t)$ denote the radioactivity concentration of the arterial $^{15}O_2$ and the total radioactivity from both

Table 1 Variables used in the recirculating water model

Symbol	*Description*	*Unit*
A_o	Radioactivity concentration of arterial $^{15}O_2$	Bq/mL
A_w	Radioactivity concentration of arterial $H_2^{15}O$	Bq/mL
A_t	Total radioactivity concentration from arterial $^{15}O_2$ and $H_2^{15}O$	Bq/mL
A_{plasma}	Radioactivity concentration of arterial plasma	Bq/mL
C	Activity concentration of $H_2^{15}O$ in peripheral tissue in a body	Bq/mL
Fi_{O_2}	Oxygen concentration in inhaled gas	%
Fe_{O_2}	Oxygen concentration in expired gas	%
k	Production rate of recirculating $H_2^{15}O$	per min
k_{BM}	Production rate of recirculating $H_2^{15}O$ obtained from BM approach	per min
k_w	Forward diffusion rate of $H_2^{15}O$ from blood to body interstitial space	per min
k_2	Backward diffusion rate of $H_2^{15}O$ from blood to body interstitial space	per min
λ	Decay constant of ^{15}O (= 0.00567 per sec)	per sec
v	Stroke volume	mL
p	k_w/k_2	
r	Respiration rate	per min
R	Fractional water content ratio in whole blood to that in the plasma	
R_{O_2}	Rate of oxidative metabolism in the whole-body system	mL/min
Δt	Delayed appearance time of recirculating water	secs
V_{O_2}	Total volume of molecular oxygen in total blood	mL
V_{TB}	Total volume of blood in a body	mL

$^{15}O_2$ and $H_2^{15}O$, respectively. $C(t)$ is an activity concentration of $H_2^{15}O$ in the peripheral tissue of the total body. Assuming a delayed appearance of RW by Δt (Iida *et al*, 1993), the following equation can be obtained:

$$A_w(t+\Delta t) = k(\alpha_1 \cdot A_t(t) \otimes \exp(-\beta_1 t) + \alpha_2 \cdot A_t(t) \otimes \exp(-\beta_2 t)) \quad (2)$$

where $\otimes$ denotes the convolution integral and:

$$\alpha_{1,2} = \frac{a - 2c \pm \sqrt{a^2 - 4b}}{\pm 2\sqrt{a^2 - 4b}}, \qquad \beta_{1,2} = \frac{a \pm \sqrt{a^2 - 4b}}{2},$$
$$a = k + k_w + k_w/p, \quad b = k \cdot k_w/p, \quad c = k_w/p, \quad p = k_w/k_2 \quad (3)$$

Following four approaches were performed to determine the rate constants and $A_w(t)$.

Approach by four parameters fitting: Four parameters, k, Δt, k_w, and p ($=k_w/k_2$), can be determined from the observed RW ($A_w(t)$) and the $A_t(t)$ curves by means of the nonlinear least square fitting (4PF approach).

Approach by one parameter fitting: Once three parameters, Δt, k_w, and p, are fixed by averaging values determined by the 4PF approach, k can then be determined by fitting the Equation 2 to measured $A_w(t)$ from $A_t(t)$ (1PF approach). In this procedure, single datum is sufficient, and thus k can be determined from $A_t(t)$ and the RW counts sampled at a single time point.

Approach from steady-state condition: Similarly to the 1PF procedures, k can be determined from the steady state condition, which is achieved by a continuous administration of $^{15}O_2$ as follows (SS approach). Incorporating the decay constant of ^{15}O ($\lambda = 0.00567$ per secs) into Equations 1a and 1b provides:

$$\frac{d}{dt}A^*_w(t) = k \cdot A^*_o(t) - k_w \cdot A^*_w(t) + k_2 \cdot C^*(t) - \lambda \cdot A^*_w(t) \quad (4a)$$

$$\frac{d}{dt}C^*(t) = k_w \cdot A^*_w(t) - k_2 \cdot C^*(t) - \lambda \cdot C^*(t) \quad (4b)$$

where variables with the symbol * denote that no correction was made for the radioactivity decay of ^{15}O. After continuously administrating $^{15}O_2$, the radioactivity distribution of $A^*_o(t)$, $A^*_w(t)$, and $C^*_t(t)$ reaches a steady state. Thus, the following equations hold:

$$0 = k \cdot A^*_o(t) - k_w A^*_w(t) + k_2 C^*(t) - \lambda A^*_w(t) \quad (5a)$$

$$0 = k_w A^*_w(t) - k_2 C^*(t) - \lambda C^*(t) \quad (5b)$$

Given the values of k_w and k_2 which are determined as averages of 4PF, k can be calculated from the arterial $^{15}O_2$ and $H_2^{15}O$ concentrations at steady state as follows:

$$k = \lambda \left(\frac{k_w + k_2 + \lambda}{k_2 + \lambda} \right) \frac{A^*_w(t)}{A^*_o(t)} \quad (6)$$

Approach by the rate of whole body oxidative metabolism: In this study, an alternative approach is provided to obtain k, from the rate of oxidative metabolism in the whole-body system (BM approach). With this alternative approach, we assume that the production rate of RW or k is proportional to the rate of oxidative metabolism in the whole-body system (i.e., $BMRO_2$ (R_{O_2}, mL/min)). The rate of oxidative metabolism may change dependent on physiologic status of the subject. In addition, we assumed that this index can be defined from the difference of oxygen concentration between inhaled and exhaled trachea air samples. Therefore, the above can be expressed as follows:

$$k = c \cdot \frac{R_{O_2}}{V_{O_2}} \text{ (per min)} \quad (7a)$$

or

$$k_{BM} = \frac{k}{c} = \frac{R_{O_2}}{1.36 \cdot Hb \cdot V_{TB}} \quad (7b)$$

where c is the proportionality constant, k_{BM} the production rate of RW obtained from BM approach, V_{O_2} (mL) the total volume of molecular oxygen in total blood, 1.36 mL/g the amount of oxygen molecules combined with unit mass of hemoglobin, Hb (g/mL) represents the hemoglobin concentration in the arterial blood, and V_{TB} (mL) is the total volume of blood in the body.

Simulation

A series of simulation studies were performed to investigate the effects of errors on estimated $CMRO_2$ value in the model parameters (k, Δt, k_w, and p). In these simulations, a typical arterial blood time activity curve (TAC) of $^{15}O_2$ and $H_2^{15}O$ after DARG protocol (Kudomi *et al*, 2005) obtained in a monkey study was used. RW TACs were generated from the whole blood TAC by assuming baseline values of k as 0.13, 0.11, 0.34, and 0.73 per min, Δt as 20, 11, 5, and 3 secs, k_w as 0.38, 0.43, 0.98, and 0.87 per min, and p as 1.31, 1.01, 0.98, and 0.83, corresponding to humans, pigs, monkeys, and rats, respectively. Tissue TACs were generated by assuming CBF = 50 mL/min per 100 g and OEF = 0.4 ($CMRO_2$ was defined as: $CMRO_2 = CBF \times OEF \times C_aO_2$, where C_aO_2 is the arterial oxygen content. This simulation was intended to investigate magnitude of error as a percentage difference, so that arbitrary value of C_aO_2 was assumed) (Hayashi *et al*, 2003), using a kinetic formula for oxygen and water in the brain tissue (Mintun *et al*, 1984; Shidahara *et al*, 2002; Kudomi *et al*, 2005). $CMRO_2$ values were calculated by the DARG method (Kudomi *et al*, 2005), in which RW TACs were separated from the whole blood by changing k from 0.0 to 1.0 per min, Δt from 0 to 30 secs, k_w from 0.0 to 2.0 per min, and p from 0.0 to 2.0, respectively. Errors in the estimated $CMRO_2$ were presented as a percentage difference from the assumed true values.

Subjects

Subjects consisted of four groups including monkeys, pigs, rats, and clinical patients. Monkeys were six healthy *macaca fascicularis* with body weight of 5.2 ± 0.8 kg and age ranging from 3- to 4-year old. Pigs were three farm pigs

with body weight of 38 ± 9 kg and age from 4 to 12 months. Rats were 12 male Wistar rats with body weight of 300 ± 54 g and age from 7 to 8 weeks. All animals were studied during anesthesia. The animals were maintained and handled in accordance with guidelines for animal research on Human Care and Use of Laboratory Animals (Rockville, National Institute of Health/Office for Protection from Research Risks, 1996). The study protocol was approved by the Subcommittee for Laboratory Animal Welfare of National Cardiovascular Center.

Human data were retrospectively sampled from an existing database at National Cardiovascular Center which documented subjects who underwent PET examination after the ^{15}O-steady-state protocol. There were 231 total samples, with body weight and age ranging from 58 ± 10 kg, and 63 ± 14 years, respectively. Only the arterial $^{15}O_2$ and $H_2^{15}O$ radioactivity concentrations measured at the steady-state condition were used for the present analysis.

Experimental Protocol

The six monkeys were anesthetized using propofol (4 mg/kg/h) and vecuronium (0.05 mg/kg/h) assigned as a baseline in contrast to the after physiologically stimulated conditions. Animals were intubated and their respiration was controlled by an anesthetic ventilator (Cato, Drager, Germany). Each monkey inhaled 2,200 MBq $^{15}O_2$ for 20 secs. After 3 mins, the monkeys were injected with 370 MBq $H_2^{15}O$ for 30 secs by the anterior tibial vein. This was aimed at assessing both CBF and $CMRO_2$ according to the DARG technique (Kudomi *et al*, 2005). At 30 secs before inhaling $^{15}O_2$ to the monkeys, arterial blood was withdrawn from the femoral artery for 420 secs at a rate of 0.45 mL/min using a Harvard pump (Harvard Apparatus, Holliston, MA, USA). The whole blood TAC was measured with a continuous monitoring system (Kudomi *et al*, 2003) and the $A_t(t)$ was obtained. Meanwhile, we also manually obtained 0.5 mL of arterial blood samples from the contralateral femoral artery at 30, 50, 70, 90, 110, 130, 160, 190, and 360 secs after the $^{15}O_2$ inhalation. For the analysis of sampled blood, 0.2 mL of the blood were used for measurement of the radioactivity concentration of the whole blood, and the rest of the blood sampled (~0.3 mL) was immediately centrifuged for separation to measure the plasma radioactivity concentration ($A_{plasma}(t)$, Bq/mL). The radioactivity concentration was measured using a well counter (Molecular Imaging Laboratory Co. Ltd, Suita, Japan).

In two monkeys, anesthetic level was changed by altering the injection dose of propofol from 4 (baseline) to 8 and then to 12 and 16 mg/kg/h in one monkey, and to 5 and then to 7, 10, and 15 mg/kg/h in the other. In another monkey, $PaCO_2$ level was varied from 39 (baseline) to 47, and then to 33, 26, and 42 mm Hg by changing the respiratory rate. Each measurement for $^{15}O_2$ inhalation and $H_2^{15}O$ injection was initiated after at least 30 mins of applying the physiologic stimulation to achieve a steady state. All procedures were the same as those for the baseline, with the exception of the manual blood sample, which was obtained only once at 70 secs.

Before and after 6 mins of the $^{15}O_2$ inhalation, oxygen concentration in both inhaled (Fi_{O_2}, %) and end-tidal expiratory gas (Fe_{O_2}, %) was measured by the anesthetic ventilator in five out of the six monkeys. Using the respiration rate (r, per min) and the stroke volume (v, mL) indicated on the ventilator, the $BMRO_2$ (R_{O_2} mL/min) was calculated using the following equation:

$$R_{O_2} = (Fi_{O_2} - Fe_{O_2}) \cdot v \cdot r.$$

All monkeys received a PET measurement to assess the $CMRO_2$ at physiologically baseline condition. The scan protocol followed the DARG technique (Kudomi *et al*, 2005) in which a 6-mins single dynamic PET scan was performed in conjunction with the administration of dual tracers (i.e., $^{15}O_2$ followed by $H_2^{15}O$ after a 3-mins interval). PET scanner used was ECAT HR (Siemens-CTI, Knoxville, TN, USA), which provided 47 tomographic slice images for an axial field-of-view of approximately 150 mm. We performed arterial–sinus blood sampling to obtain a global OEF (OEF_{A-V}) (A–V difference approach). We sampled 0.2 mL of arterial and sinus blood simultaneously during each PET scan and measured their oxygen content (C_aO_2 and C_vO_2, respectively) (Kudomi *et al*, 2005). The OEF_{A-V} was calculated as: $OEF_{A-V} = (C_aO_2 - C_vO_2)/C_aO_2$.

With regards to the farm pigs involved in this experiment, we used existing data, which were originally obtained in one of the myocardial projects. During the study, three farm pigs were anesthetized. Anesthesia was induced by ketamine (10 mg/kg) and maintained using propofol (4 mg/kg/h). Animals were intubated and their respiration was controlled by the anesthetic ventilator. Venous blood was labeled with $^{15}O_2$ using a small artificial lung unit (Magata *et al*, 2003). $^{15}O_2$-labeled blood (222 to 700 MBq) was injected for 10 secs via anterior tibial vein. At 30 secs before this injection, arterial blood was withdrawn from the femoral artery at a rate of 0.45 mL/min using the Harvard pump and continued for 420 secs. The whole blood TAC ($A_t(t)$) was then measured with a continuous monitoring system (Kudomi *et al*, 2003). Meanwhile, we manually sampled 0.5 mL of arterial blood from the contralateral femoral artery at 30, 60, 90, 90, 120, 180, 240, and 300 secs after the $^{15}O_2$-labeled blood injection. For the analysis of sampled blood, 0.2 mL of the blood were used for measurement of the radioactivity concentration of the whole blood, and the rest of the blood sampled (~0.3 mL) was immediately centrifuged for separation to measure the plasma radioactivity ($A_{plasma}(t)$, Bq/mL). The radioactivity was measured using the well counter.

Data for rats were also originally obtained for other projects, and only the blood counts were used in this study. Anesthesia was induced with pentobarbital (50 mg/kg). A 10 mL of venous blood was labeled $^{15}O_2$ using a small artificial lung unit as described previously (Magata *et al*, 2003), and approximately 1 mL of $^{15}O_2$-labeled blood (37 to 74 MBq) was injected for 30 secs via the tail vein. Arterial blood samples of 0.1 mL each were obtained from the femoral artery at 5-secs intervals for 60 secs and 10-secs intervals for another 60 secs after the injection. Whole blood radioactivity concentration was measured using the well counter to be used as $A_t(t)$. Arterial blood samples of

0.2 mL each were obtained at 30, 60, 90, and 120 secs, and the plasma radioactivity concentration ($A_{plasma}(t)$) was measured by the well counter.

For clinical patients, the blood radioactivity concentration was obtained from previously performed PET examinations, which followed the steady-state protocol (Hirano *et al*, 1994). Each patient inhaled both $^{15}O_2$ and $C^{15}O_2$ to reach the steady state with an inhalation dose of approximately 1,200 and 500 MBq/min, respectively. Five to seven arterial blood samples were obtained during the steady state from the brachial artery. Mean values of radioactivity concentration of the whole blood and plasma, $A_t(t)$ and $A_{plasma}(t)$, respectively, were obtained for both $^{15}O_2$ and $C^{15}O_2$ PET examination.

Data Analysis

Using the blood activity data obtained from monkeys, pigs, and rats at baseline conditions, k as well as Δt, k_w and p were first determined by the 4PF approach, in which Equation 2 was applied to fit the $A_w(t)$ using the observed $A_t(t)$. Because the solubility of the oxygen is negligibly small in the plasma, we assumed that all radioactivity in plasma fraction comes from $H_2^{15}O$ and that the water content ratio of whole blood to plasma (R) does not change during measurement, which means that the kinetics of water molecules immediately reach equilibrium between the plasma and the cellular fraction (Mintun *et al*, 1984; Iida *et al*, 1993). Thus, $A_w(t)$ was obtained from the equation: $A_w(t) = A_{plasma}(t) \cdot R$, where R value was obtained from the sampled blood at the end of the scan (at which all the radioactivity in the blood can be considered as coming from $H_2^{15}O$ because inhaled $^{15}O_2$ is all metabolized).

Given that the values of Δt, k_w, and p were averages determined from 4PF for monkeys, pigs, and rats, only k was determined by fitting Equation 2 to A_w. This was calculated at various points in time, more specifically, in 30, 50, 70, 90, 110, 130, 160, and 190 secs for monkeys, in 30, 60, 90, 90, 120, 180, and 240 secs for pigs, and in 30, 60, 90, and 120 secs for rats. The optimal time point for k under the 1PF approach was determined, so that $(k_{4PF} - k_{1PF})/k_{4PF}$ reaches a minimal value. Here, k_{4PF} and k_{1PF} denote k values determined by the 4PF and 1PF approaches, respectively. The values of k in monkeys at baseline condition, together with those in pigs and rats were compared between 4PF and 1PF approaches, in which a k value from the optimal single time point was used.

In three of the monkeys, which were physiologically stimulated, k of 1PF approach was obtained using single time point of A_w. Assuming the total blood volume (V_{TB}) for monkeys as 360 mL (Lindstedt and Schaeffer, 2002), and using Hb as measured value in each experiment, k_{BM} was calculated from R_{O_2} according to Equation 7b. Then, k_{BM} obtained as: $k_{BM} = 0.00204 R_{O_2}$ was compared with k determined by 1PF.

For clinical data obtained from the steady-state (SS approach) PET examinations, Equation 6 was used to determine the k values of the SS approach for each patient, in which values of k_w and k_2 were 0.38 and 0.29 per min as obtained in a previous work by Huang *et al* (1991).

$CMRO_2$ and OEF values in monkeys at baseline condition were calculated using the RW TACs obtained by four different methods (i.e., directly measured $A_w(t)$ ($n = 6$), 4PF ($n = 6$), 1PF ($n = 6$), and BM approaches ($n = 5$)). Regions-of-interest were selected for over the whole brain, and $CMRO_2$ and OEF values were obtained in those regions-of-interest. The $CMRO_2$ values compared among the four methods mentioned above to estimate RW TACs. The Bland–Altman method was applied to analyze the agreement of OEF values between the methods. Also, OEF values were compared with OEF_{A-V}.

All data were presented as mean ± 1 standard deviation. Student's t-test was used and Pearson's regression analysis was applied to compare two variables. A probability value of < 0.05 was considered statistically significant.

Results

Figure 1 shows results from the simulation study, and shows the magnitude of errors in $CMRO_2$ calculated by the DARG method as well as errors in the parameters, k, Δt, k_w, and p. Errors in $CMRO_2$ were most sensitive to errors in k amongst all species, namely the production rate constant of RW in the arterial blood. After errors in k, errors in $CMRO_2$ were sensitive to errors in Δt. Errors in k_w and p, however, appeared to cause relatively insignificant errors in $CMRO_2$. More specifically, only 5 to 10% errors are caused in $CMRO_2$ by a change of ± 50% in k_w and p.

Figures 2A–2C show examples of the arterial whole blood curves (A_t) and RW TAC (A_w) observed in typical studies on a monkey, a pig, and a rat, respectively. The RW curves became constant after a period in all species. The rise time or appearance of the RW curves, $A_w(t)$, was significantly delayed compare to that of whole blood curve, $A_t(t)$. $A_w(t)$ curves fitted by 4PF well reproduced the measured RW curves in three species: monkeys, pigs, and rats. Table 2 summarizes values of k, Δt, k_w, and p obtained by the four parameter fitting (4PF approach), at the baseline for monkeys, pigs, and rats, and also k value obtained by the steady-state formula for clinical patients. Those comparisons showed that the k was significantly different among species ($P < 0.001$) except between pig and human subjects, and it was significantly lower in smaller animals. Likewise, Δt showed significant differences among the three species ($P < 0.001$), and it was also lower in smaller animals.

Table 3 summarizes k and $CMRO_2$ values obtained from a series of PET experiments performed on six monkeys at baseline condition, and for increased anesthesia (in two monkeys), and changed $PaCO_2$ levels (in one monkey). The best agreement of k values between 4PF and 1PF approaches was obtained from the blood sample data taken at 60, 70, and 60 secs in pigs, monkeys, and rats, respectively, and was used in the 1PF approach. With this